Annals of Nuclear Energy 110 (2017) 603–612

Contents lists available at ScienceDirect

Annals of Nuclear Energy

journal homepage: www.elsevier.com/locate/anucene

Quasi-differential elastic and inelastic neutron scattering from iron in the MeV energy range ☆

A.M. Daskalakis [a,b,*], E.J. Blain [a], B.J. McDermott [a,b], R.M. Bahran [a], Y. Danon [a], D.P. Barry [b], R.C. Block [b], M.J. Rapp [b], B.E. Epping [b], G. Leinweber [b]

[a] Gaerttner LINAC Center, Rensselaer Polytechnic Institute, Troy, NY 12180, United States
[b] Naval Nuclear Laboratory, KAPL, P.O. Box 1072, Schenectady, NY 12301, United States

ARTICLE INFO

Article history:
Received 14 April 2017
Received in revised form 6 July 2017
Accepted 7 July 2017

ABSTRACT

Scattering experiments performed with the Rensselaer Polytechnic Institute Linear Accelerator measured elastic and inelastic scattering from an elemental iron sample. Eight liquid scintillator (EJ-301) proton recoil fast neutron detectors were positioned at several angles 0.5 m from the scattering sample. Data were measured using neutron time-of-flight in the energy range from 0.5 to 20 MeV, and pulse shape analysis was used to discriminate neutrons from gamma-rays. Nuclear data evaluations were compared to experimental data using Monte Carlo calculations. Below 2 MeV two new techniques were developed: a method which assessed inelastic-to-elastic scattering ratios and a method to determine the contribution from neutrons after only elastic scattering. These techniques, along with time-of-flight results, may help identify specific reactions that account for differences between evaluations and experimental data.

1. Introduction

^{56}Fe was identified as an isotope where the accuracy of nuclear data is crucial for design and operation of Gen IV reactors (Aliberti et al., 2006). ^{56}Fe is the most abundant isotope of iron (≈92%) (NNDC, 2014), which is the main element for steel alloys. Steel is a commonly used structural material for many nuclear applications such as reactor pressure vessels that serves as the primary containment for the nuclear fuel. During operation the reactor pressure vessel is exposed to a high neutron flux. Therefore, it is important that models accurately quantify neutron interactions in the pressure vessel. However, a simulation is only as accurate as base assumptions used to create it. Regarding nuclear data, deviations in the magnitude of the inelastic scattering cross section will harden or soften the neutron flux spectrum.

The abundance and importance of ^{56}Fe has allowed for many measurements of its nuclear properties, specifically inelastic scattering (e.g., Loef and Lind, Kiehn and Goodman, and Day (Van Loef and Lind, 1955; Kiehn and Goodman, 1954; Day, 1956). Recent experiments utilized high purity germanium detectors (Beyer et al., 2014; Negret et al., 2014) to infer the first few inelastic levels from the experimental gamma-ray data. Inelastic neutrons from natural iron were directly measured at Argonne National Laboratory using a pulsed monoenergetic neutron source (Smith and Guenther, 1979). Experimental data are used with nuclear models to develop evaluated nuclear data evaluations such as ENDF/B-VII.1 (Chadwick et al., 2011), JEFF-3.2 (OECD-NEA, 2015), and JENDL-4.0 (Shibata et al., 2011).

At Rensselaer Polytechnic Institute (RPI) the neutron scattering system was used to measure neutrons that scattered from a thick sample. Experimental data were compared with Monte Carlo simulations to benchmark different nuclear evaluations and their sensitivity to the scattering cross sections (elastic and inelastic) and to their angular distributions. Discrepancies between calculations and data found in the region-of-interest (ROI), 0.5–20 MeV, were used to determine regions where different nuclear data evaluations may be improved. These measurements have been referred to as "quasi-differential" because neutrons may have undergone multiple scatterings. Details of the RPI neutron scattering system and its pros and cons with respect to integral and differential neutron scattering measurements have been previously discussed (Saglime et al., 2010; Saglime, 2009; Barry et al., 2013). Previously measured materials include beryllium (Saglime, 2009), molybdenum (Saglime, 2009), zirconium (Barry et al., 2013), and ^{238}U (Daskalakis et al., 2014).

☆ The submitted manuscript has been authored by a contractor of the U. S. Government under contract No. DE-NR-0000031. Accordingly, the U. S. Government retains a non-exclusive, royalty-free license to publish or reproduce the published form of this contribution, or allow others to do so, for U. S. Government purposes.

* Corresponding author at: Naval Nuclear Laboratory, KAPL, P.O. Box 1072, Schenectady, NY 12301, United States.
E-mail address: adamdaskalakis@gmail.com (A.M. Daskalakis).

http://dx.doi.org/10.1016/j.anucene.2017.07.007
0306-4549/

Two new methodologies were developed to extract the contribution of inelastic neutrons and elastic neutrons from time-of-flight (TOF) measurements. Both methods relied on in-beam measurements to develop distinct energy-dependent detector response functions. Response functions are the result of two parameters from each neutron event: their TOF and the amount of energy deposited in the EJ-301 detector. Neutron TOF was used to calculate incident energy, and the area under each pulse formed the distribution relative to a specific incident neutron energy. Detector response functions were then used to determine the ratio of inelastic-to-elastic detected, scattered events and the elastic scattering contribution.

2. Methods

2.1. Experimental setup

The sample-of-interest for the measurements was elemental iron, or ^{Nat}Fe, and the experimental setup was nearly identical to the setup used for the ^{238}U measurement (Daskalakis et al., 2014) (illustrated in Fig. 1). The RPI Linear Accelerator (LINAC) was operated at 400 pulses per second, had an average electron current of 8 μA, and an electron burst width of 7 ns. Electrons accelerated to 53 MeV were incident on a neutron producing tantalum target (Overberg et al., 1999) that created bremsstrahlung radiation, which further interacted with tantalum to produce a continuous energy neutron distribution modeled as an evaporation spectrum (Saglime, 2009). A 1.9 cm thick depleted uranium filter was placed in the neutron beam to reduce the gamma-flash intensity. Neutrons were collimated along an evacuated flight path and were incident on a scattering sample located 30.07 m from the target. Along a separate flight path (approximately 9 m from the neutron producing target) moderated fission chambers monitored fluctuations in the neutron beam intensity.

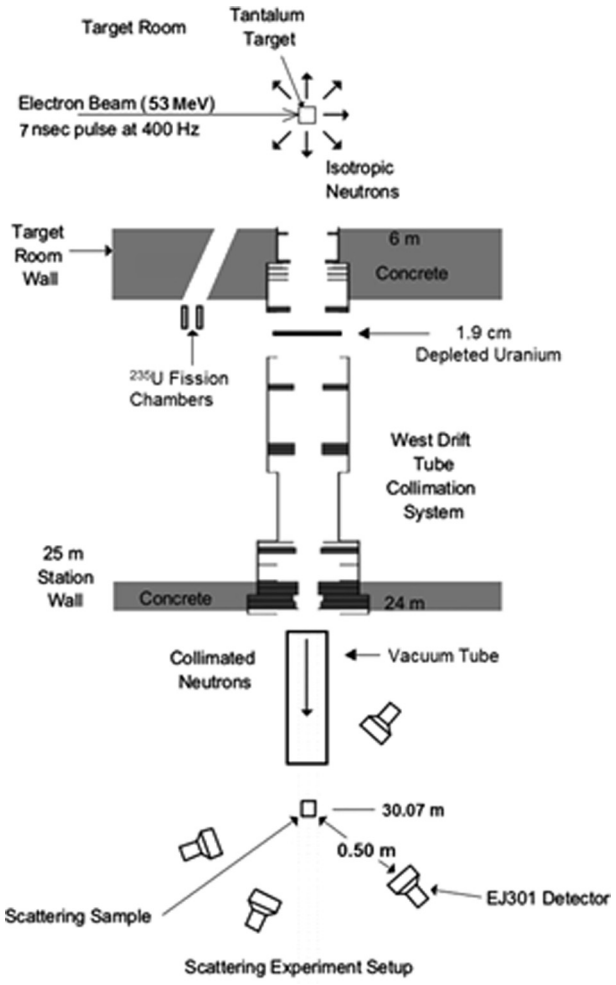

Fig. 1. Illustration of the RPI neutron scattering system (Saglime et al., 2010). A pulsed neutron beam produced by the RPI LINAC travelled 30.07 m along a collimated evacuated flight path. Neutron scattering measurements were made using the TOF technique. Note: This figure is not to scale and only four out of eight EJ-301 detectors are shown.

Eight Eljen Technologies EJ-301 (ElJEN Technologies, 2016) liquid scintillator proton recoil fast neutron detectors were used for the iron measurements. Each liquid scintillator measured 7.62 cm thick by 12.7 cm diameter and was coupled to a 12.7 cm diameter Photonix XP4572/B photomultiplier tube (PMT). A CAEN unit (model 1733 N) supplied negative high voltage to each PMT and was used to adjust their gain. The gain was optimized for neutron energies in the ROI (Saglime, 2009). Throughout the ^{Nat}Fe scattering measurement, the gain of each detector was aligned and periodically checked with the Compton edge of 0.511 MeV annihilation gamma-rays from a ^{22}Na source. The detectors were arranged at predetermined scattering angles relative to the incident neutron beam based on discrepancies between nuclear data evaluations of ^{56}Fe. Typically, two detectors were placed at the same scattering angle (different azimuthal angles). Care was taken to maximize the distance between detectors to minimize cross talk (Barry et al., 2013).

Detector electric pulses were digitized by an Agilent-Acqiris AP240 8-bit digitizer that operated with 1 GHz sampling rate. Digitized pulses were transferred by an onboard field programmable gate array if the pulse exceeded a predefined threshold (Saglime, 2009). Each detector signal consisted of a sequence of 120 1 ns samples, selected to match the EJ-301 liquid scintillator response time. Although the data acquisition system was capable of providing 128,000 transfers per second (Saglime, 2009), an average of only 3200 transfers per second occurred during the ^{Nat}Fe neutron scattering experiment.

Digitized pulses were classified as either a neutron or a gamma-ray based on pulse shape classification (PSC). PSC compared the digitized pulse with reference neutron and gamma-ray pulse shapes, and each digitized pulse was then classified based on best agreement (Daskalakis, 2015). To improve the PSC performance with small detector pulses a gamma misclassification correction (GMC) was included as part of the data analysis process (Daskalakis et al., 2014). The GMC was used to correct the neutron counts by subtracting a fraction of the measured gamma-rays that account for those that were erroneously classified as neutrons (Daskalakis, 2015). In past measurements the GMC reduced the neutron contribution by a maximum of ~3% in some energy regions (Daskalakis et al., 2014).

2.2. Iron samples

The iron scattering sample consisted of two rectangular pieces with dimensions of 15.25 cm in height by 3.85 cm in width (perpendicular to the incident beam) by 3.23 cm thick (in the beam axis). Piece 1 weighed 1475.9 g and piece 2 weighed 1475.5 g, and were placed adjacent so that their total width was 7.7 cm, which is larger than the neutron beam at the scattering sample location (Saglime et al., 2010). The iron sample was positioned to minimize the scattering contribution from structural material used to support the iron sample. Both iron pieces had threaded penetrations which allowed for structural support.

The iron scattering sample was modeled as a single solid piece (length, width, and height specified in the preceding paragraph)

with its natural isotopic abundances, and with a total mass of 2985 g. Iron's natural density (7.87 g/cm^3) was used for all calculations. Mass spectroscopy was used to quantify the iron sample's impurities, and the results are shown below in Table 1. These impurity levels were judged to be insignificant, and the sample was treated as pure elemental iron in the Monte Carlo N-Particle (MCNP) Goorley et al., 2012 model.

3. Neutron time-of-flight

3.1. Data analysis methods and time-of-flight calculations

Neutron TOF, or the time required for a neutron produced in the target to travel to a detector's surface, was used to estimate a neutron's incident energy onto a scattering sample. For this experiment the total flight path consists of two parts: from the neutron production target to the center of the scattering sample, and from the midpoint of the scattering sample to the surface of the EJ-301 detector. For the RPI neutron scattering system the total physical flight path length is $L = 30.07 + 0.50 = 30.57$ m. The uncertainty in L was estimated to be about 0.005 m, based on measurements between the neutron target and scattering sample (Saglime, 2009). Broadening due to the distribution of neutron flight path lengths was accounted for by the MCNP simulation. The time in bin i, t_i, was used to estimate the neutron's initial energy, E_i, from Eq. (1).

$$E_i \cong E(t_i) = m_n c^2 \cdot \left(\left(\sqrt{1 - \left(\frac{L}{c \cdot t_i} \right)^2} \right)^{-1} - 1 \right), \tag{1}$$

where the rest mass energy for a neutron is $m_n c^2$, and c is the speed of light. Although detectors are located at specific scattering angles it is assumed that only single elastic collisions occur with nuclei and that the collisions result in minimal energy loss for the neutron. This is generally true for nuclei with mass greater than ≈10 times the neutron mass.

All MCNP simulations were performed in the time domain so that the calculated response was modeled to mimic the recorded experimental data. Eq. (1) was used to approximate the incident neutron's energy for both experiments and MCNP simulations.

Throughout the experiment several sets of data were collected by cycling samples into and out of the pulsed neutron beam using a programmable sample changer. Scattering samples were placed on low mass sample holders to limit the scattered background neutron contribution from the sample holders. Previous work showed that dead-time effects were negligible for neutron scattering experiments (ElJEN Technologies, 2016). Background was determined from an open beam measurement while scattering samples were positioned away from the neutron beam path. The net number of measured scattered neutron counts, $C_{i,j}$, in a TOF equivalent energy bin i for detector j were determined by subtracting the open beam counts, $D^O_{i,j}$, from the sample counts, $D^S_{i,j}$. The GMC for the sample and open beam, $G^S_{i,j}$ and $G^O_{i,j}$ respectively, were used to correct for erroneously classified gamma-rays as shown in Eq. (2). As with previous experiments, the GMC correction peaked at approximately 3% near incident neutron energies of 5 MeV. Below 5 MeV the GMC contribution was less than 1%.

$$C_{i,j} = (D^S_{i,j} - G^S_{i,j}) - (D^O_{i,j} - G^O_{i,j}) \cdot \frac{M^S}{M^O} \tag{2}$$

Fluctuations in neutron beam intensity and measurement times were corrected for by adjusting the open beam contribution by the ratio of monitor counts measured with the sample in, M^S, to monitor counts measured with the open beam, M^O.

The statistical uncertainty in the number of neutron counts, $\Delta C_{i,j}$, associated with Eq. (2), was calculated with standard error propagation formula for uncorrelated variables (chapter 3 of Knoll (2000)).

$$\Delta C_{i,j} = \sqrt{D^S_{i,j} + G^S_{i,j} + D^O_{i,j} \cdot \left(\frac{M^S}{M^O} \right)^2 + G^O_{i,j} \cdot \left(\frac{M^S}{M^O} \right)^2 + M^S \cdot \left(\frac{D^O_{i,j} - G^O_{i,j}}{M^O} \right)^2 + (D^O_{i,j} - G^O_{i,j})^2 \cdot \left(\frac{M^{S^2}}{M^{O^3}} \right)} \tag{3}$$

MCNP simulations were compared with experimental data using a figure-of-merit (FOM) shown in Eq. (4). The FOM has the same functional form as reduced chi-square goodness of fit and was applied to incident neutrons energies in the ROI. The differences between experimental data and normalized MCNP calculation, $M_{i,j}$, were calculated for each TOF equivalent energy bin, i, and detector, j. The evaluation with the lowest FOM was considered to have best agreement with the experimental data.

$$\mathrm{FOM}_j = \frac{1}{n} \cdot \sum_{i=0.5\mathrm{MeV}}^{20\mathrm{MeV}} \frac{(C_{i,j} - M_{i,j})^2}{\varepsilon^2_{i,j}}, \tag{4}$$

where the total number of energy bins in the ROI is represented by n. Experimental uncertainties, $\varepsilon^2_{i,j}$, shown in Eq. (5), include the statistical uncertainty for an energy channel, $\Delta C_{i,j}$, and the systematic uncertainty represented by the fractional normalization factor, ε_N. Eq. (5) defines the uncertainty at each energy bin for each detector.

$$\varepsilon^2_{i,j} = \Delta C^2_{i,j} + (C_{i,j} \cdot \varepsilon_N)^2 \tag{5}$$

A high purity graphite reference sample was used to determine the normalization factor (Daskalakis et al., 2014). The normalization uncertainty, ε_N, was calculated from the difference between experimental data and MCNP simulations for each detector. Graphite was selected due to good agreement among carbon evaluations (ENDF/B-VII.1 Chadwick et al., 2011 and JEFF-3.2 (OECD-NEA, 2015). Agreement between experimental graphite data and MCNP calculations served as verification of the data analysis and modeling methodology. Differences were attributed to systematic uncertainties that encompass experimental uncertainties with the neutron energy-dependent flux shape and the EJ-301 detector's energy-dependent neutron efficiencies.

Table 1
Impurities for both pieces of the iron sample. Only impurities greater than 0.01% are listed.

Element	Piece 1 [%]	Piece 2 [%]
S	0.023	0.024
As	0.010	0.013
Mn	0.030	0.030
Ni	0.090	0.100
Mo	0.030	0.030
Cu	0.120	0.120
Sn	0.017	0.017
Si	0.020	0.010

3.2. Neutron time-of-flight (TOF) measurements

Detector angles presented in Table 2 and displayed in Figs. 2 through 5 are relative to the incident neutron beam and have an uncertainty of ±2°. Fig. 2 displays the measured data from the graphite reference sample and the predicted MCNP calculated response. All graphite FOM, calculated with Eq. (4), are significantly lower than the ^{Nat}Fe FOM, which indicates that the differences between ^{Nat}Fe experimental data and each evaluation vary beyond systematic uncertainties.

Table 2
Experimental iron data compared with MCNP calculations using the FOM from Eq. (4). The FOM was calculated for incident neutron energies in the ROI. The lowest FOM representing best fitting evaluations are shown in bold text; multiple selections indicate evaluations that are statistically indistinguishable. Detector angle uncertainty is ±2°.

Angle	Detector	Experiment	ENDF/B VII.1	JENDL 4.0	JEFF 3.2	Graphite ENDF/B-VII.1
30	7	2	24.64	**19.79**	49.96	3.69
45	7	1	12.24	**9.02**	15.68	2.11
61	2	1	9.46	**8.40**	9.54	1.31
77	2	2	**14.74**	**15.22**	17.43	2.40
111	5	2	18.34	**12.95**	19.38	3.92
109	6	2	22.65	**14.51**	21.62	4.42
130	5	1	9.13	**6.36**	11.84	2.94
130	6	1	10.07	**7.78**	13.60	2.09
153	3	1	**16.33**	**16.80**	21.95	3.00
153	3	2	25.88	**23.37**	39.79	4.92
156	4	1	**17.96**	**18.56**	23.21	3.70
156	4	2	**28.59**	**29.26**	47.25	5.19
Average	–	–	17.50	**15.17**	24.27	3.31

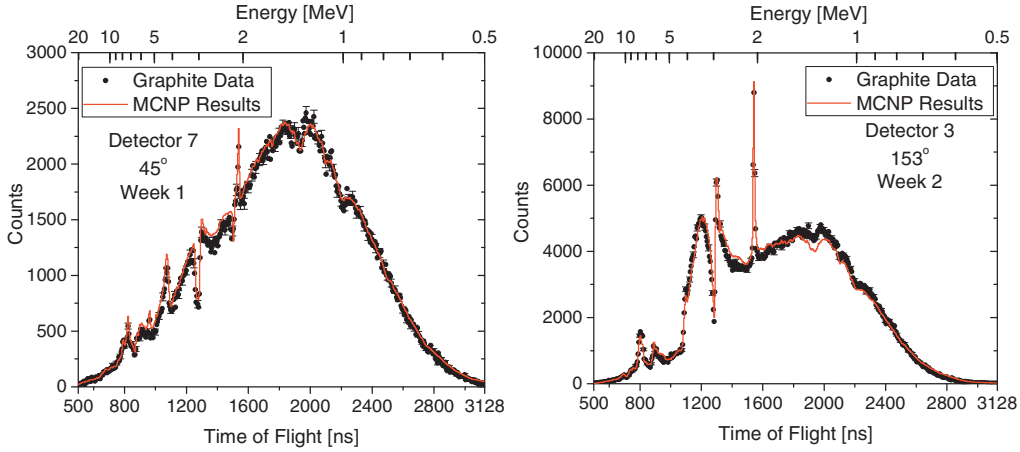

Fig. 2. The measured response from the graphite reference sample by detector 7 (left) and detector 3 (right) located at 45° and 153°, respectively. Differences between measured data and MCNP calculations were used to calculate the systematic uncertainties.

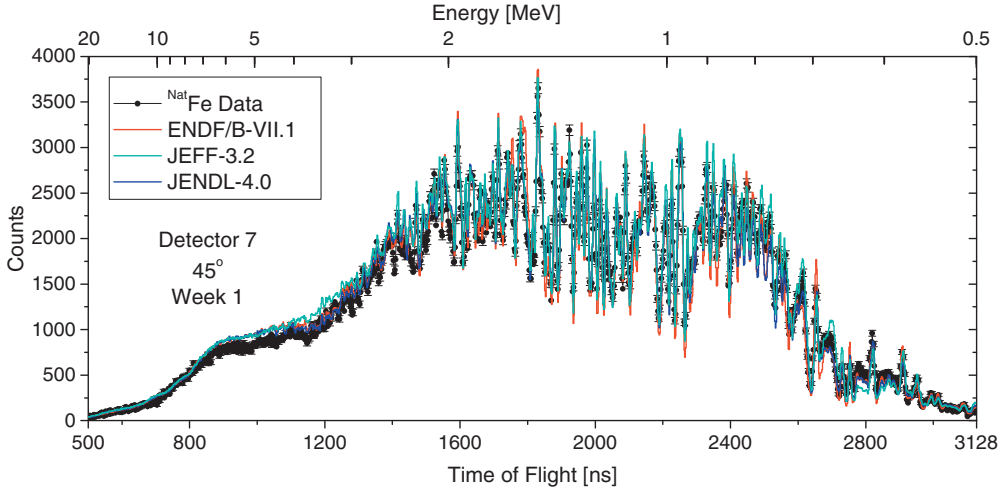

Fig. 3. Detector 7 located at 45° during the first experiment. Over the entire ROI (from 0.5 to 20 MeV) the JENDL-4.0 evaluation has the best agreement with the experimental data.

Table 2 lists the FOM from the iron measurement for three evaluations in columns 4 through 6. These results are from twelve combinations of detectors and angles, and the averages over all twelve values are listed at the bottom of the table. The lowest iron FOM and all FOMs that are within 0.7 of that value are listed in bold type. The 0.7 sensitivity value was determined by adjusting the experimental data by its calculated uncertainty and recalculating the FOM (Daskalakis et al., 2014). The FOM values for a specific

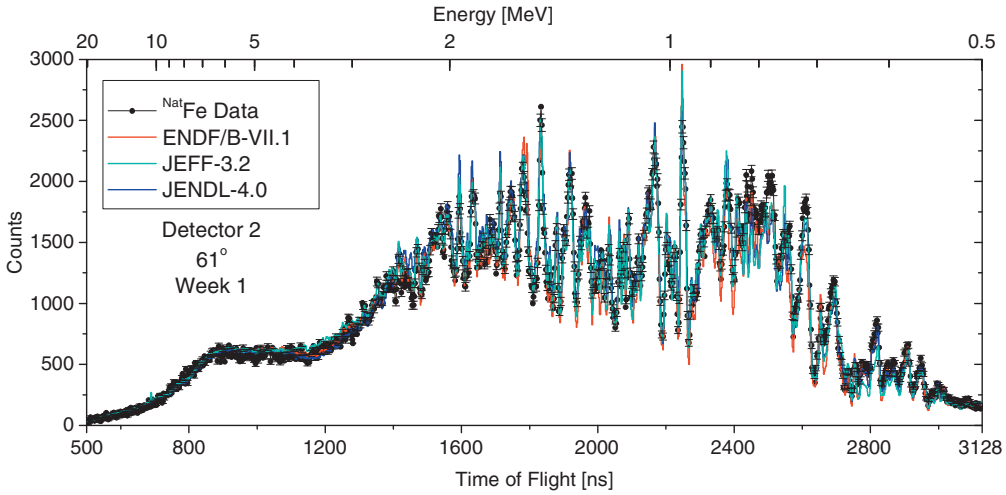

Fig. 4. Detector 2 located at 61° during the first experiment. Over the entire ROI the JENDL-4.0 evaluation has the best agreement with the experimental data.

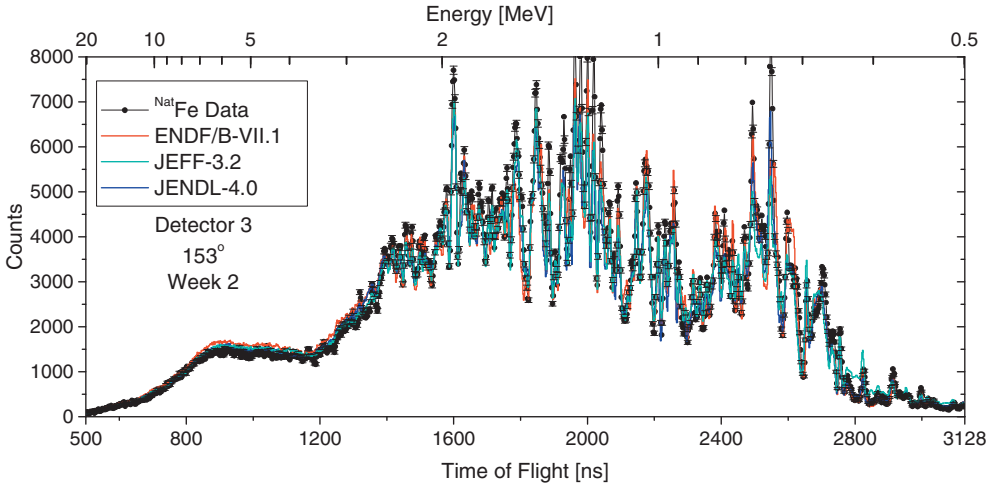

Fig. 5. Detector 3 located at 153° during the second experiment. Over the entire ROI the JENDL-4.0 evaluation has the best agreement with the experimental data.

nuclear evaluation and detector can only be compared with other FOM values for that same detector and experiment; however, overall conclusions regarding best fitting libraries for detectors at similar angles can be directly compared.

The JENDL-4.0 evaluation was in agreement (within the 0.7 sensitivity band) with all twelve measurements. For detectors located at 30°, 45°, 61°, 109°, 111°, and 130° (both detectors) the JENDL-4.0 evaluation was the only one in agreement with the experimental data. At back angles of 153° and 156° the FOM for the JENDL-4.0 evaluation was slightly higher than the ENDF/B-VII.1 evaluation, but still within the uncertainty band established by the sensitivity analysis. Examination of results below 1 MeV found the JENDL-4.0 evaluation to have good agreement with experimental data; however, poor agreement was observed between 1.5 and 2.0 MeV. Additionally, the JENDL-4.0 ^{Nat}Fe evaluation's calculated FOM were significantly higher than the calculated FOM for the graphite reference, which indicates that there is room for improvement of the iron evaluation.

The FOM calculated with the ENDF/B-VII.1 evaluation was in agreement with four detectors located at 77°, 153° (first experiment), and 156° (both experiments). For both experiments, detectors 3 and 4 (located at back-scattering angles of 153° and 156° respectively) had better agreement with the ENDF/B-VII.1 evaluation than with the JENDL-4.0 evaluation. However, an exception occurs with detector 3, in the second experiment, where the JENDL-4.0 agreement is slightly better.

The JEFF-3.2 evaluation had the poorest agreement with the experimental data. A unique and original study performed to assess the elastic scattering contribution from 1.5 to 2.0 MeV found good agreement between the JEFF-3.2 evaluation and the experimental data (Daskalakis, 2015). However, the FOM calculated over the entire ROI found that the JEFF-3.2 evaluation did not reside within the range for best fitting libraries at any angle. This was caused by poor agreement below 1 MeV (see Fig. 3).

Experimental data and MCNP calculations are shown for detectors at 45° (detector 7), 61° (detector 2), and 153° (detector 3) in Figs. 3 through 5.

4. Inelastic-to-elastic ratios

4.1. Spectrum unfolding analysis and calculations

Neutrons deposit their energy within a detector primarily by transferring their energy to a recoiling proton. Energy deposited by each neutron varies based on its incident energy, which also affects the amount of light production in the EJ-301 scintillator. For monoenergetic neutrons a spread in energy can be observed

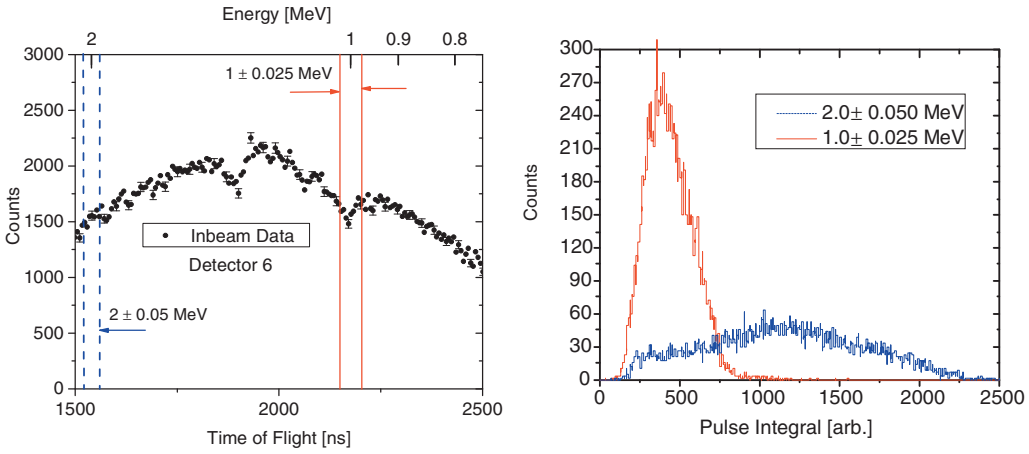

Fig. 6. Neutron in-beam data from an EJ-301 detector with two energy bins (left) isolating 1.0 MeV (solid red vertical lines) and 2.0 MeV (dashed blue vertical lines) neutron TOF. Only neutron events in these bins were used to develop response functions R(1.0) and R(2.0), which have distinct distributions (right). Pulse integral is proportional neutron energy deposition and is displayed in arbitrary units. (For interpretation of the references to colour in this figure legend, the reader is referred to the web version of this article.)

based on this distribution. To characterize the energy of the scattered neutron distinct energy-dependent response functions, R(E), were generated based on experimental in-beam measurements.

Experiments to measure R(E) for each detector were performed by placing each EJ-301 neutron detector into the neutron beam at the scattering sample position and running the RPI LINAC at the same electron beam energy as in the scattering experiment but with low average power (Daskalakis et al., 2014). Data were separated into sixteen energy bins for neutron energies between 0.5 and 2.0 MeV (bin spacing of 0.1 MeV), based on neutron TOF. The resolution of each bin was selected to be ±2.5% of the incident neutron energy (e.g., E_i = 2 ± 0.05 MeV), which provides sufficient resolution in time to capture all neutrons generated with the energy of that bin (i.e., approximately ± 20 ns, or ± 0.01 MeV, for incident 2 MeV neutrons). The distribution of neutron energies in each bin was determined by summing the energy deposition of each neutron depositing energy at that time-of-flight. The pulse integral was defined as a pulse's integrated area, which was proportional to the energy deposited by the neutron in the scintillator. The energy bins and resulting response functions are shown in Fig. 6. Fig. 6(left) displays the 1.0 MeV (solid red vertical lines) and 2.0 MeV (dashed blue vertical lines) neutron TOF equivalent energy bins. The distribution for the 1.0 and 2.0 MeV energy bins, displayed in Fig. 6 (right), are distinguishable and are defined as response functions R(1.0) and R(2.0), respectively.

Linear interpolation was used to produce any R(E) that fell between two measured values, e.g., R(1.95) was calculated with the R(1.9) and R(2.0). Interpolation fidelity is discussed in reference 19, and is used to calculate a response function for any neutron energy between 0.5 and 2.0 MeV.

At each time bin Eq. (1) was used to determine E_i. This was used to calculate the elastic and inelastic neutron energies, E_{el} and E_{in} respectively, using Eq. (6).

$$E_{el,in} = \frac{\left[\mu \cdot \sqrt{E_i} + \sqrt{E_i \cdot (\mu^2 + M^2 - 1) + M \cdot (M+1) \cdot Q}\right]^2}{(M+1)^2}, \tag{6}$$

where $\mu = \cos(\theta)$, M is the atomic mass of the target nuclei (≈55.85), and Q is the nucleus excitation state (Q = 0 MeV for elastic collision, Q = 0.847 MeV for the first inelastic state of ^{56}Fe). Energies for both elastic and inelastic response functions were calculated with Eq. (6). Limitations of EJ-301 detectors to measure low energy neutrons prevent measurement of neutrons below 0.5 MeV. Therefore, inelastic neutrons were only measured if the scattered neutron's incident energy was 1.3 MeV or greater.

As an example, Fig. 7 displays the pulse height distribution from E_i = 2 ± 0.05 MeV that scattered from the ^{Nat}Fe sample to a detector positioned at 153° (relative to the incident neutron beam). The ^{Nat}Fe scattering data (black) are represented as a superposition of two distinct distributions. An elastic (blue) response function and inelastic (red) response function were calculated and overlaid on the scattering data. The energy after an elastic or inelastic collision was calculated with Eq. (6) to be $E_{el} \approx 1.9$ MeV and $E_{in} \approx 1.1$ MeV, respectively.

Below 2 MeV only the first inelastic state of ^{56}Fe contributes to the inelastic response function. Contributions from other iron isotopes were negligible for this energy region (Daskalakis, 2015). Response functions were linearly fit to the ^{Nat}Fe scattering data's pulse height distribution using:

$$C(E_i) = A \cdot \mathrm{R}_{el}(E_1) + (1 - A) \cdot \mathrm{R}_{in}(E_2) \;\; 0 \leqslant A \leqslant 1 \tag{7}$$

where A is the fraction of neutrons that contributed to the elastic response function. The value A was also used to find the experimental inelastic to elastic ratio, I/E, at each energy bin.

$$\mathrm{I/E} = \frac{(1 - A)}{A} \tag{8}$$

Eqs. (7) and (8) were used for the fit displayed in Fig. 8. The experimental I/E ratio was not used to calculate the ratio between inelastic and elastic differential cross sections, but rather the measured reaction rate in discrete energy bins, which can be compared to simulations.

The I/E uncertainty consists of both statistical and systematic uncertainties. Statistical uncertainties from the elastic response function, inelastic response function, and scattering data are each calculated with Eq. (3) then root summed squared. The systematic uncertainty is derived using the graphite reference sample (Daskalakis et al., 2014). And the uncertainty for A was derived in reference (Daskalakis, 2015). The uncertainty components are summed for conservatism.

All MCNP I/E calculations were performed such that their statistical uncertainties were negligible (more than 2 orders of magnitude smaller than the experimental data's statistical uncertainty). A library is in good agreement with the experimental data if it lies within the experimental data's uncertainty.

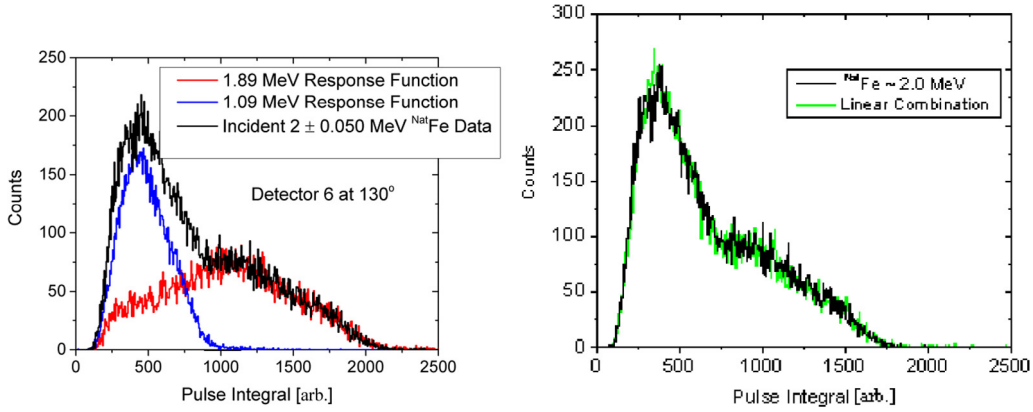

Fig. 7. The neutron pulse height distribution for $E_i = 2 \pm 0.05$ MeV that scattering from a ^{Nat}Fe sample to a detector positioned located at 153° with elastic (blue) and inelastic (red) response functions overlaid on the scattering data (left). A linear combination of the elastic and inelastic response function was used to calculate I/E ratios for the 2 MeV incident neutrons (right). (For interpretation of the references to colour in this figure legend, the reader is referred to the web version of this article.)

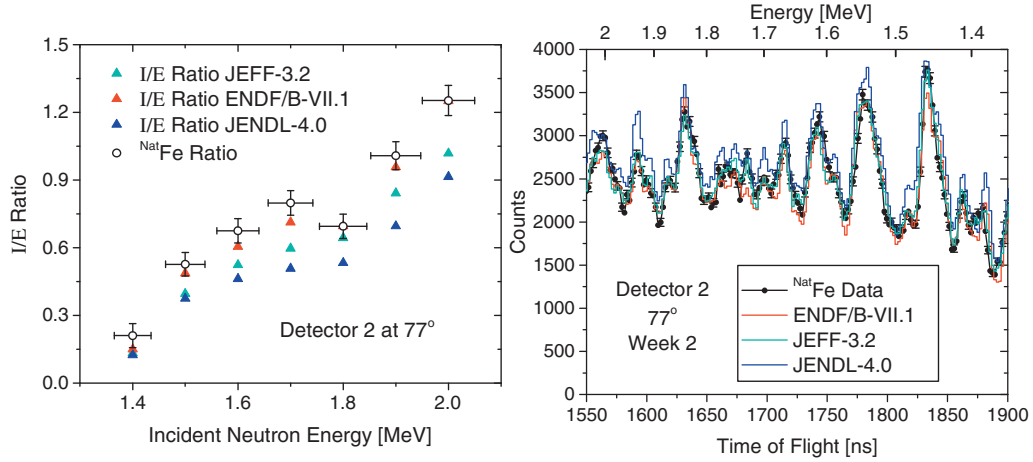

Fig. 8. I/E ratios (left) and TOF data (right) for detector 2 at 77° for incident neutrons between 1.4 and 2 MeV. The ENDF/B-VII.1 evaluation was within experimental uncertainties at three energy bins. All data were collected during the second experiment.

4.2. Experimental inelastic-to-elastic ratio

Figs. 8 and 9 show the results vs. energy bin for two different scattering angles. In this energy range the differential data still contain strong resonance structure, which was averaged for energy bins used for I/E ratios. The neutron angular distribution depends on the resonance parameters and thus also exhibits fluctuations that are also typically smoothed out by the evaluations (using larger energy bins). This type of averaging could be the source of some of the deviations observed.

Simulations with the ENDF/B-VII.1 evaluation compared best to experimental data. This was in contrast to the FOM results where the JENDL-4.0 evaluation had the best agreement in the ROI. It was found that two factors contributed to this difference: the limited number of bins analyzed for each incident neutron energy, and that the JENDL-4.0 evaluation does not perform well in TOF for this energy region. Above 1.0 MeV the JENDL-4.0 evaluation overestimates the scattering contribution (see Fig. 9), which was attributed to elastic scattering (Daskalakis, 2015). Similarly, the JEFF-3.2 evaluation had the poorest performance among the three evaluations; however, examining TOF data only in the range from 1.4 to 2.0 MeV showed that it closely matched the experimental data. This indicates that the disagreement observed between TOF data and I/E ratios could be the result of the limited number of bins used to assess incident neutron energies.

Figs. 8 and 9 display I/E ratios and the TOF for energies between 1.4 and 2.0 MeV. In some cases, the calculated I/E ratios are within experimental uncertainties whereas the TOF data and evaluations have stark differences. In these instances, the TOF data and experimental I/E ratios should be used together to assess the angular distribution of scattered neutrons from ^{Nat}Fe

5. Elastic scattering only

To separate elastic-only scattering another analysis technique was derived from detector response functions and by application of an energy dependent discriminator (EDD).

5.1. Energy dependent discriminator

This method was used to eliminate the contribution of inelastic neutrons at each time bin, thereby providing a method to quantify only the elastic scattering contribution for each detector. This is possible because the maximum energy an inelastic scattered neutron can deposit in a detector is less than the energy an elastically scattered neutron can deposit.

The EDD was applied by locating the end point for each response function. A third order polynomial was fit to the end point locations as a function of incident neutron energy, and an example is shown in Fig. 10.

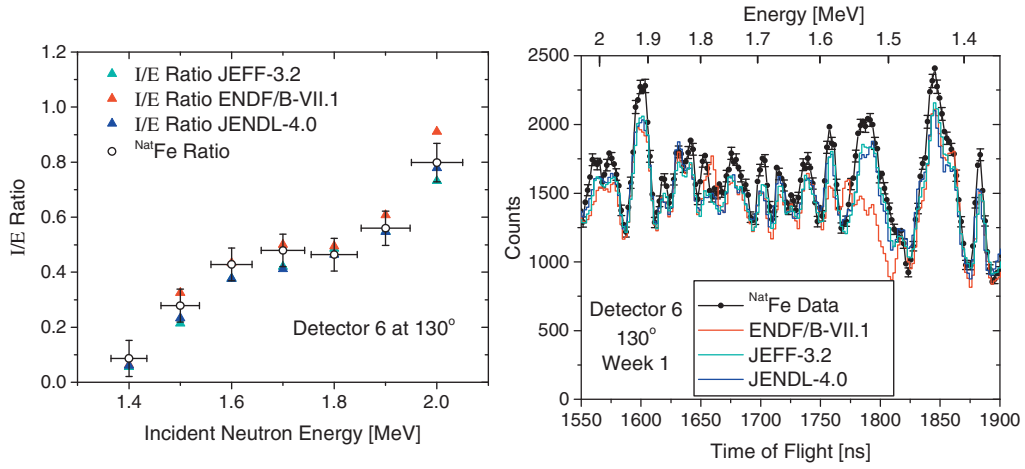

Fig. 9. I/E ratios (left) and TOF data (right) for detector 6 at 130° for incident neutrons between 1.4 and 2 MeV. The three evaluations were within experimental uncertainties for six energy bins. All data were collected during the first experiment.

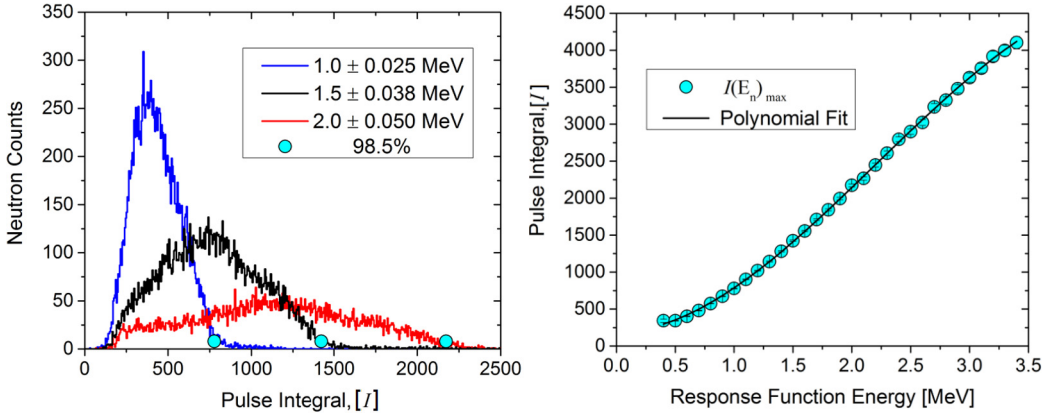

Fig. 10. Three response functions with cyan circles representing the channel where each response function ends (left). A third order polynomial fit to the end point locations as a function of response function energy (right). (For interpretation of the references to colour in this figure legend, the reader is referred to the web version of this article.)

Table 3
FOM values for the different ^{Nat}Fe evaluations assessing only their elastic contribution in the energy range between 1.4 and 2.0 MeV. Lowest FOM values, or those that are statistically indistinguishable (Daskalakis et al., 2014), are shown in bold text.

Angle	Detector	Experiment	ENDF/B VII.1	JENDL 4.0	JEFF 3.2	Graphite ENDF/B-VII.1
30	7	2	15.69	17.41	**5.11**	0.77
45	7	1	7.75	**4.98**	**4.65**	0.70
60	2	1	**3.05**	6.80	**3.66**	0.71
77	2	2	**2.73**	22.52	6.00	0.65
111	5	2	13.15	5.41	**3.65**	1.24
109	6	2	13.07	**4.32**	**3.76**	3.43
130	5	1	3.54	**1.68**	**0.59**	2.06
130	6	1	4.45	**1.55**	**0.81**	1.39
153	3	1	8.95	8.04	**4.00**	1.63
153	3	2	24.85	19.49	**8.44**	1.95
156	4	1	8.94	8.80	**3.74**	3.31
156	4	2	22.18	18.80	**6.88**	3.59
Average	–	–	10.70	9.98	**4.27**	1.79

From Eq. (6) the inelastic and elastic scattering energy at each time bin were calculated, e.g., for 2 MeV neutrons scattered to a detector located at 130° the elastic and inelastic energies are 1.87 MeV and 1.07 MeV, respectively. Using the polynomial fit, all neutrons that deposited less energy than the inelastic response function's end point were discriminated against. A correction based on detection efficiency and the discriminator's location was applied to the experimentally elastic-only TOF spectrum, and is necessary for comparisons with the simulations. Reference (Daskalakis, 2015) outlines this method in further detail.

Calculations were normalized to the experimental data in the same manner as in Section III and Eq. (4) was used to assess how well the ^{Nat}Fe evaluations performed. However, the range was limited from 1.4 MeV to 2.0 MeV due to an increase in the response function's statistical uncertainty (Daskalakis, 2015).

5.2. Energy dependent discriminator results

The results of applying the EDD, when combined with the I/E ratios, may provide insight regarding the reaction that may be con-

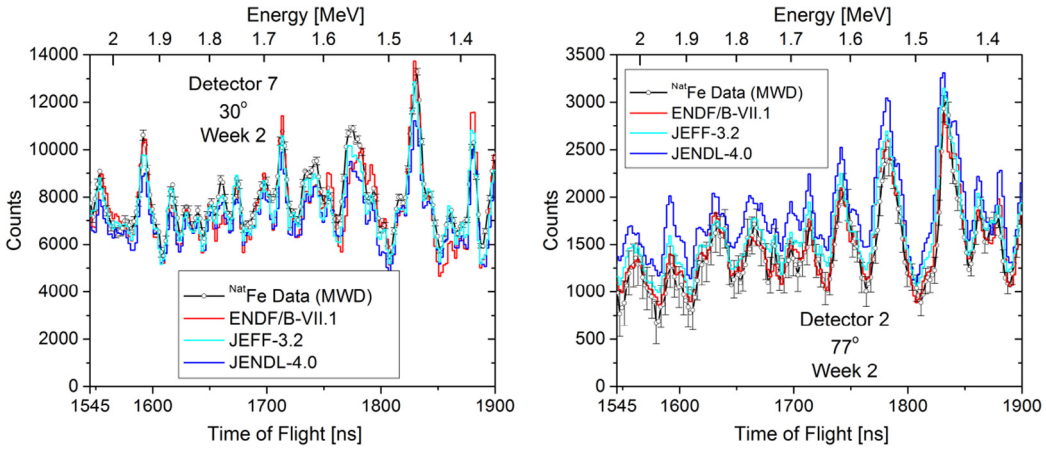

Fig. 11. Experimental data processed to consist of only elastic scattering and MCNP simulations for detectors positioned at 30° and 77°. At 30° the JEFF-3.2 evaluation has the best agreement, whereas the ENDF/B-VII.1 evaluation had better agreement at 77°.

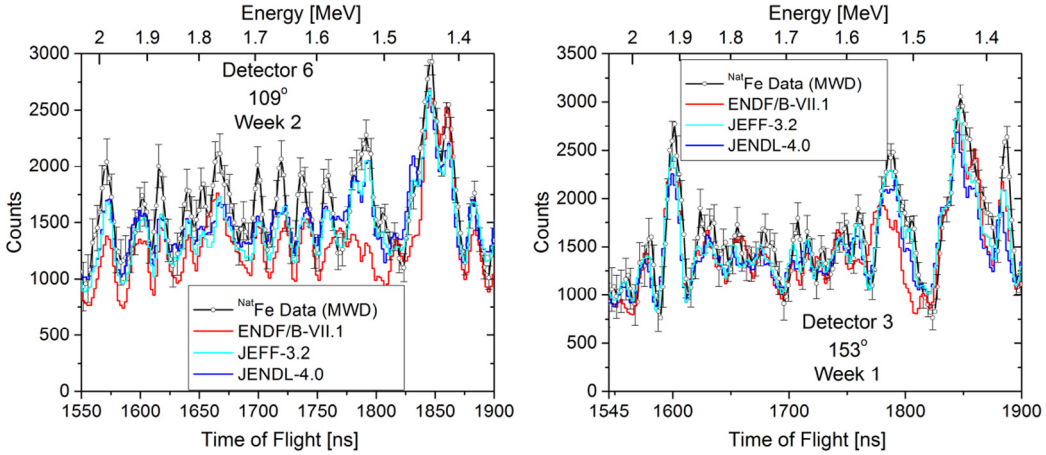

Fig. 12. Experimental data processed to consist of only elastic scattering and MCNP simulations for detectors positioned at 109° and 153°. Both the JEFF-3.2 and the JENDL-4.0 evaluations had good agreement at 109°, whereas the JEFF-3.2 evaluation had better agreement at 153°.

tributing to discrepancies between calculations and measurements. As with the TOF FOM calculation, a sensitivity study was performed, and all evaluations with a FOM within 1.4 of the best fitting evaluation are considered statistically indistinguishable. The graphite reference sample's FOM was reassessed between energies of 1.4 and 2.0 MeV. An average value of 1.8 was calculated, which indicates that the calculation and experimental data have better agreement in this energy range than throughout the entire ROI (0.5–20 MeV). This was expected because the total number of neutron counts was significantly higher for both scattering and in-beam measurements that significantly reduced statistical uncertainty for low count rates (Table 3).

The results show that the JEFF-3.2 evaluation had the best agreement with the experimental data for ten of the twelve measurements. The FOM was twice as low as the other evaluations for this energy range. This result contradicts the total TOF FOM results presented earlier; however, the differences between experimental data and the JEFF-3.2 evaluation below 1 MeV contribute to a larger FOM over the entire ROI. These results are in agreement with the I/E ratios, which do not favor any particular evaluation at forward angles and show that at back angles all evaluations perform well. Figs. 11 and 12 show the elastic only scattering contribution for two detectors.

6. Conclusion

Three unique analysis methods were demonstrated with the ^{Nat}Fe scattering data: TOF measurement between 0.5 and 20 MeV, I/E ratios, and elastic-only scattering. Experimental data were directly compared with MCNP simulations performed with the ENDF/B-VII.1, JENDL-4.0, and JEFF-3.2 evaluations. Over the entire ROI the TOF measurement assessed with the FOM had the best agreement with the JENDL-4.0 evaluation. All the ^{Nat}Fe FOM were larger than the graphite FOM, suggesting that improvements to all iron evaluations may be made.

Experimental I/E ratios showed that the ENDF/B-VII.1 evaluation had the best agreement for energy bins between 1.4 and 2.0 MeV. However, when this result was used with the elastic only data the results favored the JEFF-3.2 evaluation. Therefore, it is important to use all the methods to isolate a particular energy region or reaction to assess its accuracy. The energy resolution of this experiment may be sufficient to constrain neutron widths and spins of ^{56}Fe resonances by using the experimental data and methods presented here.

As a result of the above conclusions it seems that a combination of the inelastic to elastic ratios of JEFF-3.2 and the total scattering cross section and angular distribution from JENDL-4.0 could pro-

duce an evaluation that will provide better agreement with this benchmark.

Acknowledgements

The authors would like to thank the RPI LINAC staff: Peter Brand, Mathew Gray, Martin Strock, and Azeddine Kerdoun. The data presented in this publication would not be possible without their time and effort.

References

Aliberti, G. et al., 2006. Nuclear data sensitivity, uncertainty and target accuracy assessment for future nuclear systems. Ann. Nucl. Energy 33, 700–733.

Barry, D.P. et al., 2013. Quasi-differential neutron scattering in zirconium from 0.5 MeV to 20 MeV. Nucl. Sci. Eng. 174 (2), 188–201.

Beyer, R. et al., 2014. Inelastic scattering of fast neutrons from excited states in ^{56}Fe. Nucl. Phys. A 927, 41–52.

Chadwick, M.B., Herman, M., Oblozinsky, P., et al., 2011. ENDF/B-VII.1 nuclear data for science and technology: cross sections, covariances, fission product yields and decay data. Nucl. Data Sheets 112 (12), 2887–2996.

Daskalakis, A.M., 2015. Measurement of Elastic and Inelastic Neutron Scattering in the Energy Range From 0.5 to 20 MeV (Ph.D. Thesis). Rensselaer Polytechnic Institute.

Daskalakis, A.M. et al., 2014. Quasi-differential neutron scattering from ^{238}U from 0.5 to 20 MeV. Ann. Nucl. Energy 73, 455–464.

Day, R.B., 1956. Gamma rays from neutron inelastic scattering. Phys. Rev. 102 (3), 767–787.

ELJEN Technologies, 2016, October, 30. *EJ-301* [Online]. Available: http://www.eljentechnology.com/index.php/products/liquid-scintillators/ej-301-ej-309. Last accessed: Oct. 30, 2016.

Goorley, T. et al., 2012. Initial MCNP6 release overview. Nucl. Technol. 180, 298–315.

Kiehn, R.M., Goodman, C., 1954. Neutron inelastic scattering. Phys. Rev. 95 (4), 989–992.

Knoll, G.F., 2000. Radiation Detection and Measurement. Wiley & Sons, New York.

Negret, A. et al., 2014. Cross-section measurements for the ^{56}Fe(n, xnγ) reactions. Phys. Rev. C 90 (3), pp. 034602-1-034602-15.

National Nuclear Data Center (NNDC) at Brookhaven National Laboratory (BNL), Website: http://www.nndc.bnl.gov, Retrieved 08-19-2014.

OECD-NEA, 2015, July 17. JEFF-3.2. [Online]. Available: https://www.oecd-nea.org/dbforms/data/eva/evatapes/jeff_32/. Last accessed September 16, 2016.

Overberg, M.E. et al., 1999. Photoneutron target development for the RPI linear accelerator. Nucl. Instrum. Methods Phys. Res. A 438 (2–3), 253–264.

Saglime, F.J., 2009. High Energy Nuclear Differential Scattering Measurements for Beryllium and Molybdenum (Ph.D. thesis). Rensselaer Polytechnic Institute.

Saglime, F.J. et al., 2010. A system for differential neutron scattering experiments in the energy range from 0.5 to 20 MeV. Nucl. Instrum. Methods Phys. Res. A 620 (2–3), 401–409.

Shibata, K. et al., 2011. JENDL 4.0: a new library for nuclear science and engineering. J. Nucl. Sci. Technol. 48 (1), 1–30.

Smith, A., Guenther, P., 1979. Scattering of MeV Neutrons From Elemental Iron. Argonne National Laboratory Report, ANL/NDM-47.

Van Loef, J.J., Lind, D.A., 1955. Measurements of inelastic scattering cross sections for fast neutrons. Phys. Rev. 101 (1), 103–113.